JOURNAL OF CATALYSIS 154, 261–275 (1995)

# Alumina-Supported Pt–Rh Catalysts

## I. Microstructural Characterization

Rollin E. Lakis,[1] Charles E. Lyman,[2] and Harvey G. Stenger, Jr.*

*Materials Science and Engineering Department and *Chemical Engineering Department, Lehigh University, Bethlehem, Pennsylvania 18015*

Received March 17, 1994; revised March 27, 1995

**Analytical electron microscopy was performed on several Pt–Rh bimetallic catalysts. All catalysts prepared for this investigation contained alloy particles, but their composition distributions varied with preparation procedure. A catalyst with approximately 1 wt% total metal content and a relative metal composition of 60 wt% Pt and 40 wt% Rh, reduced at 300°C for 12 h, displayed a bimodal particle composition distribution with particle compositions centered at approximately 10 wt% Pt and 90 wt% Pt. Few particles possessed the expected average composition of 60 wt% Pt. The same catalyst when reduced at 700°C for 72 h displayed a broad particle composition distribution centered at about 60 wt% Pt. Together, these composition distributions and those observed for several other catalysts are consistent with the presence of a low-temperature miscibility gap in the Pt–Rh equilibrium phase diagram. Catalysts were also prepared that were observed to contain only Pt-rich or only Rh-rich particles. High-resolution electron microscopy identified two discrete particle morphologies, particles >7 nm in diameter were faceted and often internally faulted or twinned, while particles <7 nm displayed no internal faults and appeared to be homogeneous, and roughly circular in cross-section. Because of the small metal particle size, X-ray photoelectron spectroscopy was unable to determine if the metal particles were uniformly alloyed or if the particle surfaces were enriched with one alloy component.**

## INTRODUCTION

When considering air pollution control catalysts, the generally accepted reason for combining platinum and rhodium is that platinum is to create an excellent catalyst for the oxidation of carbon monoxide and hydrocarbons, while rhodium displays a high activity for the reduction of nitric oxide to nitrogen (1). These metals display complementary properties and are, therefore, commonly found together in automotive exhaust catalysts. In automobiles, supported Pt–Rh catalysts typically operate in the temperature range between 700 and 1000°C. However, platinum and rhodium also display significant activities for the reduction of nitric oxide below 300°C (2–10). In this temperature regime Pt–Rh catalysts could reduce cold-start emissions in automobiles, and they show promise for the low-temperature control of nitric oxide and carbon monoxide produced by electric power utilities.

Bimetallic catalysts have received a great deal of research attention in the past two decades. Although, as early as 1950, investigations were conducted on conventional metal alloys. These studies focused upon catalytic activity as a function of variations in electronic structure caused by alloying (11–15). Alloys of group VIII and group IB metals received particular attention for their activities towards hydrogenation, dehydrogenation, and isomerization. The behavior of Cu–Ni alloys were studied with respect to the hydrogenolysis of ethane to methane (15–17). Cu was observed to segregate to the surface of bulk Cu–Ni alloys and dramatically reduce the hydrogenolysis activity of the alloy. The loss of hydrogenolysis activity was attributed to a decrease in the number of Ni multiplet sites that were believed to be responsible for the reaction.

In these early investigations the alloys were prepared as systems with low dispersions, often in the forms of wires or gauzes. However, interests have shifted toward highly dispersed systems. In 1973 Sinfelt introduced the concept of bimetallic clusters to explain the interaction of two virtually immiscible metals (18). Sinfelt concluded that, in the highly dispersed state, there is a strong interaction between the degree of dispersion and the stability of nonequilibrium structures and metal distributions. Therefore, catalyst compositions are not restricted to those combinations of metals which form bulk alloys, and the properties of catalytic activity and reaction selectivity are not restricted to the simple additive properties of the individual constituents.

A barrier to the development of highly dispersed bimetallic catalysts is the absence of data on the relationships between the microstructural state and kinetic perfor-

---

[1] Present address: Laboratory for Research on the Structure of Matter, 3231 Walnut Street, Philadelphia, PA 19104-6202.

[2] E-mail: cell@lehigh.edu.

0021-9517/95 $12.00

mance of bimetallic systems. When discussing bimetallic systems, the composition of individual catalytically active particles must be considered. Do the two metals in the bimetallic system form alloy particles? Are the alloy particles better catalysts than the unalloyed components? Are they worse? These obvious questions concerning bimetallic catalysts have been left largely unanswered.

Electron probe microanalysis studies conducted on automobile catalysts have concluded that platinum and rhodium are both present throughout the active regions in fresh and vehicle aged catalyst (19, 20). Supported Pt–Rh catalysts are reported to contain alloyed platinum and rhodium particles as determined by X-ray diffraction (8), extended X-ray adsorption fine structure (6), infrared spectroscopy (21), and scanning transmission electron microscopy (19, 20, 22, 23). It is therefore agreed that when Pt and Rh are impregnated into the same support material, by a variety of impregnation techniques and precursors, alloy particles are formed.

If alloy particles are observed, the possibility of one component segregating to the surface of the alloy particles must be considered. The surface of bulk Pt–Rh alloys are observed to be enriched with Pt after high-temperature annealing in vacuum (24–28). When single crystal alloy surfaces were exposed to oxygen, Rh surface enrichment was observed (29). Several investigators used various techniques to show that when platinum–rhodium alloy particles do exist, their surface composition is strongly dependent upon their gas-phase environment and temperature history (8, 30–36). All studies confirm that under oxidizing conditions and at most temperatures, Pt–Rh alloy particles become surface enriched in rhodium. Also, some studies suggest that such rhodium exists as $Rh_2O_3$. The methods used to make this observation included reaction rate studies (8, 31), temperature-programmed desorption and chemisorption (30), surface characterization, including X-ray photoelectron spectroscopy (XPS) and auger electron spectroscopy (32–35), and transmission electron microscopy (TEM) analysis (36). Scanning transmission electron microscopy observed a modest Pt surface enrichment in a Pt–Rh alloy particle that was reduced in $H_2$ at 500°C (22).

In those characterization studies which relied upon techniques that do not possess high spatial resolution (temperature-programmed desorption, X-ray photoelectron spectroscopy, chemisorption, and kinetic studies), the compositions of individual alloy particles were not determined. Often, it was assumed that all particles were present at the same composition and that this average composition is what would be expected from the complete alloying of the constituent metals. There is no experimental evidence to support this assumption; but, without such evidence, the results of many characterization experiments cannot be interpreted.

In the present study we report on the characterization of Pt and Rh bimetallic catalysts by analytical electron microscopy, high-resolution transmission electron microscopy, and X-ray photoelectron spectroscopy. Emphasis is placed upon the measurement and interpretation of the composition-size distribution of individual catalyst particles in the size range of 2–15 nm in diameter. The composition-size distribution of several catalysts will be examined, and the utility of this construction for the elucidation of the relationships between catalyst preparation and the resulting catalyst microstructure will be demonstrated. A companion paper (37) discusses the catalytic performance of these same catalysts.

## EXPERIMENTAL

### *Catalyst Preparation*

Aqueous solutions of Pt and Rh were prepared from $PtCl_4$ (99.9%, Johnson Matthey) and $RhCl_3\ xH_2O$ (99.9% Johnson Matthey), respectively. These precursors were impregnated into γ-alumina (Corning Celcor EX78) which was ground and sieved to between 90 and 150 μm in diameter. The physical properties of this support material are summarized in Table 1 (38). The aqueous precursor concentrations required to prepare a specific metal concentration were calculated assuming the precursor solutions would completely fill the pores of the support material, and that the metal which was imbibed into the pores would remain after further processing. Typical precursor concentrations were in the range of $10^{-5}$ mole metal/cc deionized water to provide total metal compositions of approximately 1 wt%. An average batch size was prepared from approximately 4 g of dry alumina. Before impregnation at atmospheric pressure and room temperature, a volume of precursor solution was prepared that was twice the volume required to fill the pores of the support material. The precursor solution was then filtered using a 1 micron nylon membrane filter and brought into contact with the γ-alumina. The resulting slurry was stirred with a glass stir bar for approximately 5 min until the color of the support material was uniform. The wet alumina was

**TABLE 1**

**Description of γ-Alumina Support Material (38)**

| Property | Value |
|---|---|
| BET surface area | 252 $m^2/g$ |
| Pore volume | 0.4959 cc/g |
| Average pore size | 4.0 nm |
| Porosity | 63% |
| Density | 1.31 g/cc |

then placed on a Buchner funnel and quickly rinsed with about 50 cc deionized water to remove excess precursor solution from the slurry. Following the rinse, the catalyst material was allowed to air-dry overnight at room temperature. Subsequent processing varied for each catalyst and will be presented in the results section.

Analysis of several catalyst preparations by electron-probe microanalysis found the metals to be homogeneously distributed throughout the individual 100-$\mu$m support particles. Following preparation, each catalyst was analyzed for total metal content by inductively coupled plasma atomic emission spectroscopy (ICPAES, Galbraith Laboratories) and given a descriptive name which contains the average relative weight concentration of Pt and Rh. For example, a catalyst which contained 1.0 wt% Pt and 0.5 wt% Rh would be designated as 67/33.

### *Dispersion Measurements*

Metallic dispersion was determined by nonstatic chemisorption using a modified Micromeritics Flowsorb II 2300. A gas sampling valve was installed to permit a reproducible 1.03-cc injection of uncontaminated adsorbing gas. This volume was always greater than the volume of gas adsorbed, and the chemisorbed volume was determined by the difference between the first and consecutive injection measurements (39).

Chemisorption was performed using hydrogen (nitrogen carrier) and carbon monoxide (helium carrier) gases. The chemisorption results are presented in terms of dispersion, which is defined in the following manner:

$$\text{Dispersion} = \frac{2 \times \text{Moles of } H_2 \text{ Chemisorbed}}{\text{Total Number of Metal Atoms}} \times 100 \quad [1]$$

$$\text{Dispersion} = \frac{\text{Moles of CO Chemisorbed}}{\text{Total Number of Metal Atoms}} \times 100. \quad [2]$$

The total number of metal atoms was calculated using the ICPAES analysis. Since these gases adsorb on both Pt and Rh, it was not possible to measure the number of Pt and Rh surface sites independently. Only the total number of surface sites could be determined.

The accuracy of this technique was verified using a Pt chemisorption standard obtained from Micromeritics. On separate days the standard material with a specified dispersion of 33.7% (±5% relative error) was measured to be 33.8 and 29.2% by CO chemisorption. A similar measurement was made using $H_2$ chemisorption which resulted in a 34.7% dispersion. Both the CO and $H_2$ measurements were within the specified range of the calibration material, and the chemisorption method was assumed to be accurate. The CO chemisorption values were used to determine the total number of metal adsorption sites for all catalysts with the exception of the Rh monometallic catalyst. Hydrogen chemisorption values were used for the Rh catalyst because of uncertainties associated with the adsorption stoichiometry of carbon monoxide on Rh (40–43).

### *Analytical Electron Microscopy*

Analytical electron microscopy was performed using a Vacuum Generators HB-501 field-emission dedicated scanning transmission electron microscope (STEM). Platinum M-series ($M\alpha$-2.051 keV) and rhodium L-series ($L\alpha$-2.696 keV) X-rays were measured using a Si(Li) energy dispersive spectrometer with a Link Systems AN10,000 X-ray analyzer. This analyzer uses a top-hat filter to strip the background intensity from the X-ray peaks. It then fits library peak-shape standards to the measured peaks and deconvolutes the peak intensities for the X-ray families involved. A sample spectrum for a 5-nm particle is presented in Fig. 1. The STEM was operated at 100 kV and at conditions to provide approximately 0.8 nA of current into an electron probe 2 nm in diameter (full width at one-tenth maximum intensity).

STEM samples were prepared for analysis by grinding the catalyst material using a mortar and pestle, ultrasonically dispersing the catalyst in methanol, and placing two drops of the suspension on a carbon-coated copper TEM grid. Alumina support particles were observed using annular dark-field imaging to locate areas of interest which contained individual metal particles for analysis (Fig. 2). The electron beam was then rastered over a 3 nm × 4 nm area on a single metal particle. When AEM is performed on individual metal particles, the resulting analysis is the average composition of the volume which the beam sampled. Since for these experiments a 2-nm probe was rastered in a 3 nm × 4 nm rectangle, particles that were less than 5 nm in diameter were sampled over their entire volume, and particles larger than 5 nm in diameter were

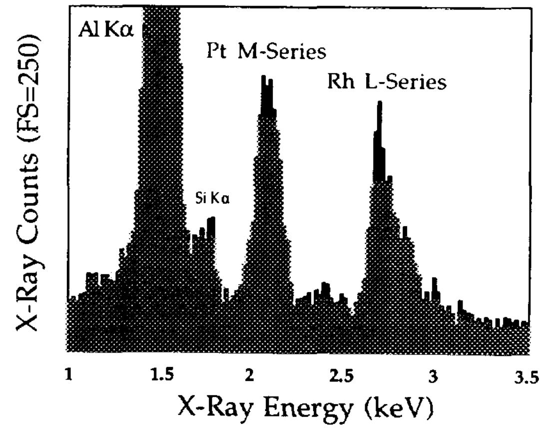

FIG. 1. X-ray spectra taken from a 4-nm alloy particle with a composition of 56 wt% Pt.

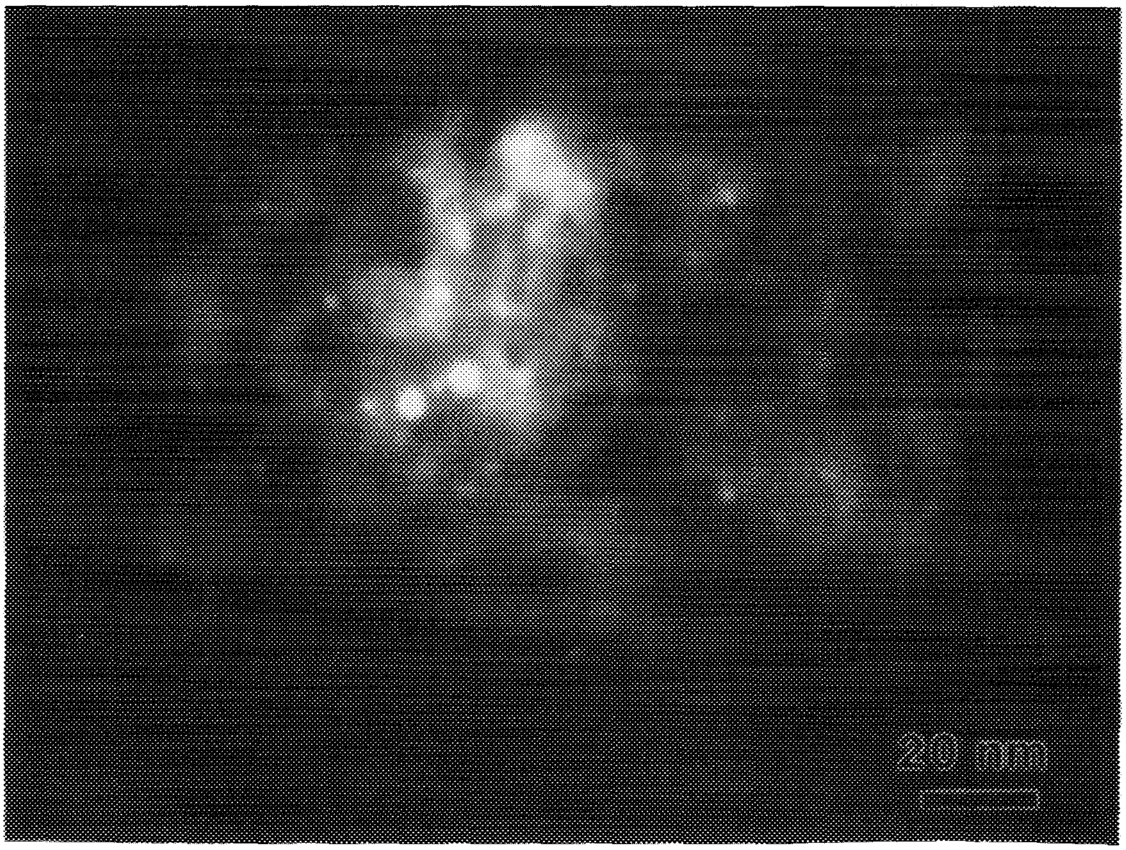

FIG. 2. Annular dark field image of a single piece of alumina which contains many metal particles.

analyzed through their centers. The analysis was performed using a rastered beam to allow direct observation of the particle during analysis. This permitted manual compensation for specimen drift and the real time observation of potential electron beam damage (44) and beam-induced contamination (45). X-rays were acquired for live times of 50 to 200 s per particle in order to achieve acceptable counting statistics (±1σ errors of 10 wt% Pt or less).

Quantification was performed using the Cliff–Lorimer ratio method (46)

$$\frac{C_{\mathrm{Pt}}}{C_{\mathrm{Rh}}} = k_{\mathrm{Pt,Rh}} \frac{I_{\mathrm{Pt}}}{I_{\mathrm{Rh}}} \quad [3]$$

where $I_{\mathrm{Pt}}$ and $I_{\mathrm{Rh}}$ are the measured X-ray intensities for Pt and Rh, $C_{\mathrm{Pt}}$ and $C_{\mathrm{Rh}}$ are the unknown weight fractions, and $k_{\mathrm{Pt,Rh}}$ is the Cliff–Lorimer $k$-factor, an experimentally determined sensitivity factor which relates the measured relative X-ray intensities to the ratio of the element weight fractions. The experimental measurement of $k_{\mathrm{Pt,Rh}}$ on a sample of known composition eliminates the need to determine difficult-to-measure parameters such as ionization cross-section and detector efficiency (47). In this investigation, the experimentally determined $k$-factor was obtained from ultramicrotomed sections of Pt–13%Rh thermocouple wire that were placed upon carbon support films. The average Cliff–Lorimer *k-factor*, $k_{\mathrm{Pt-Rh}}$ = 1.079 ± 3%, was subsequently used for quantification.

When analyzing individual metal particles, the thin film approximation was invoked, which assumes the effects of X-ray absorption and fluorescence may be ignored. In this case, the approximation was supported by X-ray absorption calculations which predicted the deviation in $k_{\mathrm{Pt,Rh}}$ caused by X-ray adsorption within a single particle (48). The effect of X-ray absorption on $k$-factors is a function of particle composition and is bounded by the effects of Pt-rich and Rh-rich particles on the generated Pt–M and Rh–L X-rays. The largest deviation in the measured $k$-factor occurs for Pt-rich particles, which if ignored will result in the apparent under estimation of the Rh concentration. A result for a 10-nm particle, which was measured to be 95 wt% Pt and 5 wt% Rh without absorption correction, after correction would become 94.8 wt% Pt and 5.2 wt% Rh (a Rh increase of 4%). The alumina support material has only a small effect on Pt and Rh X-ray absorption: an alumina thickness of 100 nm leads to a deviation in $k_{\mathrm{Pt,Rh}}$ which results in the apparent under estimation of

Pt concentrations. An uncorrected 50 wt% Pt particle in 100 nm of alumina would actually be 51 wt% Pt when corrected for absorption. Since the Pt–Rh *k*-factor was measured as a function of specimen thickness, and the effects of X-ray absorption as a function of particle composition and diameter are known, it is possible to explicitly correct for these effects for each particle analyzed. However, the systematic error introduced by the thin film approximation is small in comparison to the X-ray statistical counting error. Therefore, the effect of X-ray absorption can be safely ignored for Pt–Rh particles less than 10 nm in diameter in approximately 100 nm of alumina.

The precision of AEM measurements is typically limited by counting statistics, and STEM measurements of individual highly dispersed catalyst particles are no exception. In many analytical situations this limitation is overcome by either making several measurements of similar specimen areas and performing confidence interval tests, or by simply counting sufficiently long in a single analysis to minimize the statistical counting error. For the dispersed catalyst materials under investigation, neither option was feasible. Each individual metal particle represents a unique analysis opportunity, multiple analyses of similar sample regions are not possible, and the maximum analysis time per particle is dictated by the buildup of specimen contamination and electron beam damage to the alumina support. The error for each composition measurement ($\pm 1\sigma$) was estimated using error propagation, assuming the standard deviation in a single measurement of a X-ray peak equals the square root of the number of X-ray counts in that peak.

To avoid biasing the AEM results by inappropriate sampling of the individual alloy particles, two selection rules were developed: no more than 10 to 15 particles were analyzed in each piece of alumina, and a range of alloy particle sizes was analyzed in each piece of alumina. This sampling procedure was not intended to provide a truly representative particle size distribution of the catalysts or an estimate of the particle dispersion. It was intended to examine the relationship between particle composition and size for those metal particles which likely formed in the 4-nm pores of the alumina support material.

### *High-Resolution Electron Microscopy*

High-resolution electron microscopy (HREM) was performed using the JEOL 4000EX transmission electron microscope at the Arizona State University Center for High Resolution Electron Microscopy. When operated at 400 keV this microscope provides, under ideal conditions, an interpretable resolution of 0.17 nm. Specimens were prepared similarly to those for AEM with the exception that the catalyst suspension was deposited upon plain copper TEM grids with no carbon support film. Areas of the specimen where small metal particles were found in thin areas of the support, or exposed off the edge of the alumina, were photographed at a direct magnification of 500,000×. After an image was captured on film, it was converted to a digital format using a CCD camera and Gatan's Digital Micrograph software running on a Macintosh Quadra 950 computer. This software can also generate a simulated diffraction pattern from selected portions of an image. From such patterns, the angles and distances between crystallographic planes may be determined. Since Pt, Rh, and their alloys are known to possess the face centered cubic structure, the lattice planes may be indexed on this basis. In some alloy systems it is possible to determine alloy composition from the lattice constants measured in HREM images, but for the Pt–Rh case, there is only a 3% change in lattice parameter over the complete composition range from pure Pt to pure Rh. This small difference is difficult to reliably detect using this technique.

### *X-Ray Photoelectron Spectroscopy*

X-ray photoelectron spectroscopy (XPS) was performed to determine the surface composition of the alloy catalysts. This work was performed using a Scienta ESCA-300 instrument, which is capable of generating a high-photon flux for rapid data acquisition. The ESCA-300 provides an energy resolution which is limited by the natural line widths of the photoelectrons under investigation. The high-photon intensity also permits the investigation of dispersed catalysts with a total metal loading of about 1 wt%. A freshly polished Pt–30 wt% Rh thermocouple wire was utilized to determine a bulk sensitivity factor of 1.267 for the intensity ratio of the Pt $4f_{7/2}$ to Rh $3p_{3/2}$ signals. This sensitivity factor was used to convert experimental XPS Pt/Rh intensity ratios to chemical compositions.

The supported catalysts were hydraulically pressed between tungsten carbide dies to produce a self-supporting sheet of the material to be analyzed. This preparation method produced a relatively smooth sample surface which displayed improved charge neutralization characteristics under the irradiation of an electron flood gun when compared to other more conventional preparation techniques. Quantification was performed using the ESCA-300 software to curve fit the data and extract integrated intensities from overlapped peaks. The Al $2p$ line directly overlaps the Pt $4f_{5/2}$ line (Fig. 3a), but the Pt $4f_{7/2}$ line could be successfully analyzed. The Rh $3p_{3/2}$ line was selected for quantification because of the absence of interfering lines (Fig. 3b). Unfortunately, the Rh $3d$ and Pt $4d$ lines are considerably overlapped, but they were monitored for lineshape changes (Fig. 4a).

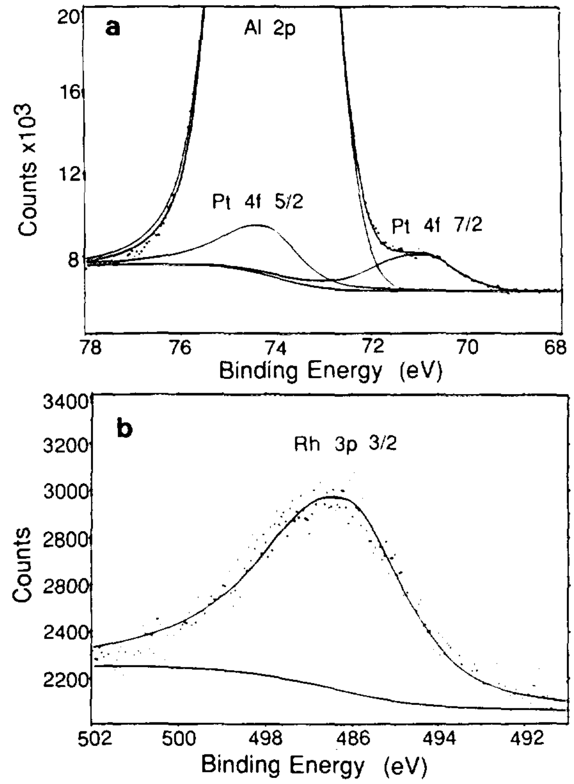

FIG. 3. Typical XPS spectra of Pt–Rh alloy catalyst materials which contains the peak models used for intensity integration and quantification: (a) Pt 4*f* region used for Pt quantification, (b) Rh 3*p* region used for Rh quantification.

Pure Pt and pure Rh spectra were also compared to the Pt–30 wt% Rh alloy standard to determine if any significant energy shifts were present due to alloying. The magnitude of the observed shifts were such that they would be easily obscured in the supported catalyst specimens by line broadening due to charging and by the lack of a reliable energy reference.

## RESULTS

While the overall procedure for catalyst preparation has been given above, the preparation of each catalyst is summarized in the following subsections (also summarized in Table 1 of Part II). The experimental results are presented in chronological order.

### *60/40 Alloy Catalysts*

This alloy catalyst was first impregnated with Pt, air-dried overnight, and then calcined in air at 500°C for 3 h. The material was then impregnated with Rh and air-dried overnight. During the final preparation step, the catalyst was reduced in flowing $H_2$ at 300°C for 12 h. The impregnation solutions were prepared to make a catalyst that would be 0.5 wt% Pt and 0.5 wt% Rh. The actual metal concentrations in the supported catalyst were 0.61 wt% Pt, and 0.40 wt% Rh, with 0.55 wt% Cl as determined by ICPAES (Galbraith Laboratories). CO chemisorption found this catalyst to be 51% dispersed. This catalyst will be referred to as the 60/40 catalyst. A portion of the 60/40 catalyst was reduced in flowing $H_2$ at 700°C for 72 h instead of 300°C for 12 h. This catalyst was labeled 60/40A. The dispersion of this catalyst was determined by CO chemisorption to be 44%.

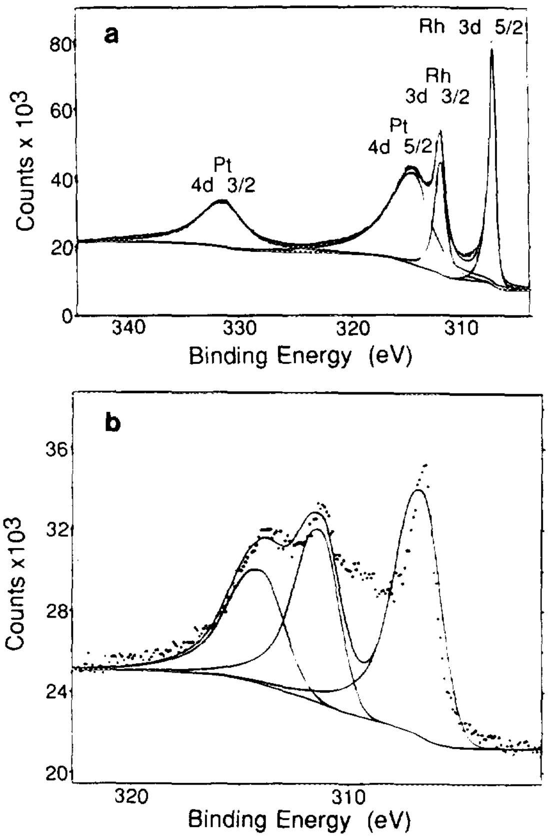

FIG. 4. XPS spectra showing the modeled peak overlap situation in the Rh 3*d*, Pt 4*d* region of the spectrum. This spectral region was used to detect lineshape changes and was not used for quantitation: (a) spectrum taken from freshly polished Pt–30 wt% Rh bulk alloy standard. Solid lines represent fitted spectra for the alloy standard, (b) Rh 3*d*–Pt 4*d* region of spectrum for the 75/25 $Rh_{ox}$–$Pt_{red}$ catalyst (dots) compared to the fitted spectrum of (a). Excess intensity between the two Rh 3*d* peaks implies mixed oxidation states.

Analytical electron microscopy results for the 60/40 catalyst after catalytic testing are presented in Fig. 5. This plot of Pt composition (Rh composition = 100-Pt composition) versus particle size for the 60/40 catalyst displays a bimodal distribution of particle compositions, with very few particles possessing the bulk composition of 60 wt% Pt. Instead, particle compositions appear to be centered at approximately 10 wt% Pt and 90 wt% Pt. A

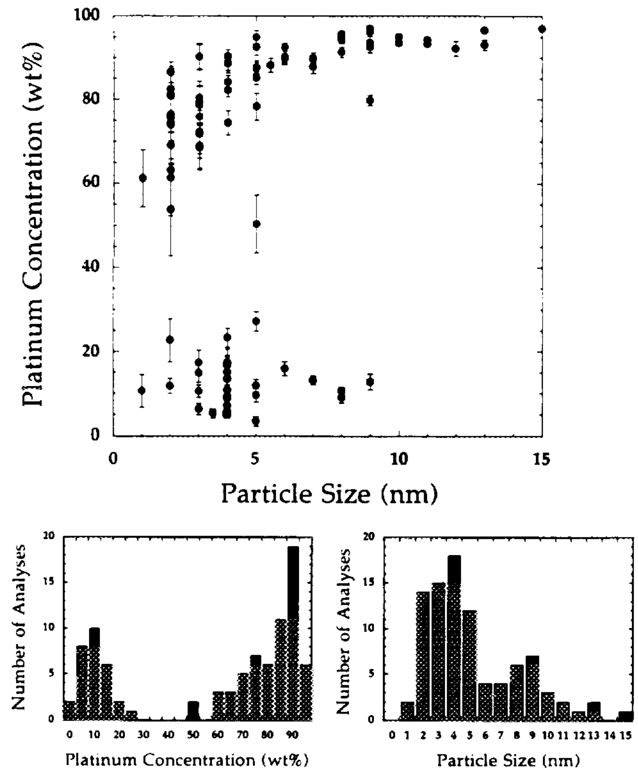

FIG. 5. Plot of particle composition versus size for the 60/40 catalyst. Particle composition and particle size histograms are also presented.

trend toward increasing Pt concentration with increasing particle size is present in the Pt-rich portion of the particle composition distribution. The Rh-rich portion of the distribution does not exhibit an obvious trend. Particles in the composition range of 20 wt% Pt to 60 wt% Pt are conspicuously absent.

AEM results for the 60/40A catalyst are presented in Fig. 6. A broad distribution of particle compositions was observed for this catalyst with a substantial fraction of all particles measured found in the 20 wt% Pt to 80 wt% Pt composition range. This is a very different particle composition distribution from that observed for the 60/40 catalyst. The 60/40 and 60/40A catalysts were prepared from the same material; the only difference was the final reduction temperature.

Atomic resolution images of the 60/40 catalysts were obtained by HREM. Both catalysts appeared similar in HREM images. Typical images of the 60/40 catalyst are presented in Fig. 7. Particles in the 1–4 nm range were roughly circular in cross-section and possessed no internal defect structure (Fig. 7A and 7B). Figure 7A contains two particles, and the calculated diffraction pattern was taken from the bottom particle. This pattern can be indexed as a [100] zone axis, and the prominent diffraction spots are {200} reflections. The calculated interplanar spacing of 1.967 Å is in good agreement with the expected spacing of 1.962 Å for Pt {200}. Figure 7B shows a particle in which cross-fringes are observed. The associated diffraction pattern is also of the [100] type with both sets of {200} reflections visible. An angle of 88.7° was measured between {200} planes, which is in good agreement with the expected value of 90°. The measured interplanar spacings, 1.992 and 2.049 Å, were also within experimental limits for Pt {200}. Particles larger than 7 nm were often faceted along crystallographic planes, and nearly always contained internal faults and twin boundaries (49). Figure 7C is a typical example of this type of particle. There were no analytical capabilities available on the TEM used for high-resolution work; therefore, no correlation between particle composition and morphology was possible. Also, since the variation of lattice parameter with alloy composition is only 3%, no compositional information could be extracted from the lattice spacings in the HREM images.

The average metal particle surface composition of the 60/40 catalyst was determined by quantitative XPS analysis to be 8 wt% Pt (92 wt% Rh). The particle composition which would be expected based upon the bulk composition of the catalyst determined by ICPAES is 60 wt% Pt. Thus, the XPS data suggest that these alloy particles are surface-enriched with Rh when compared to the expected bulk composition.

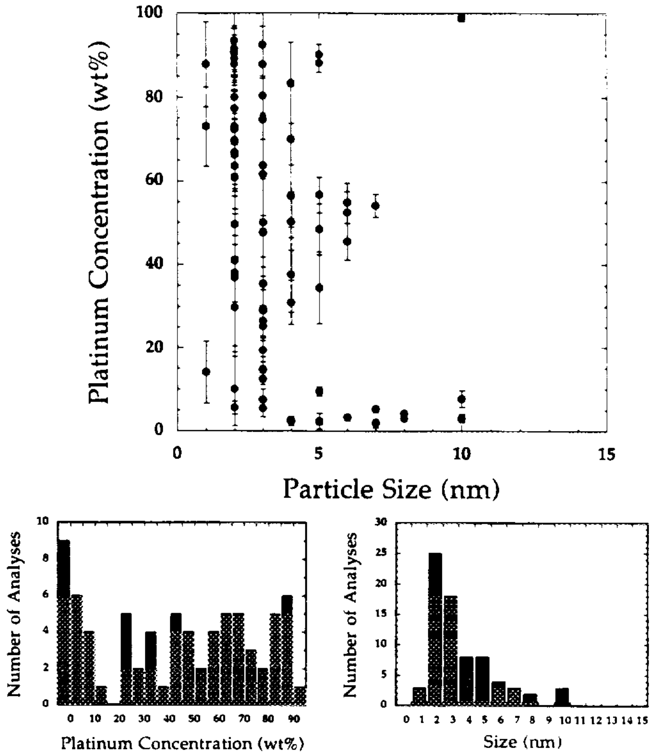

FIG. 6. Plot of particle composition versus size for the 60/40A catalyst. Particle composition and particle size histograms are also presented.

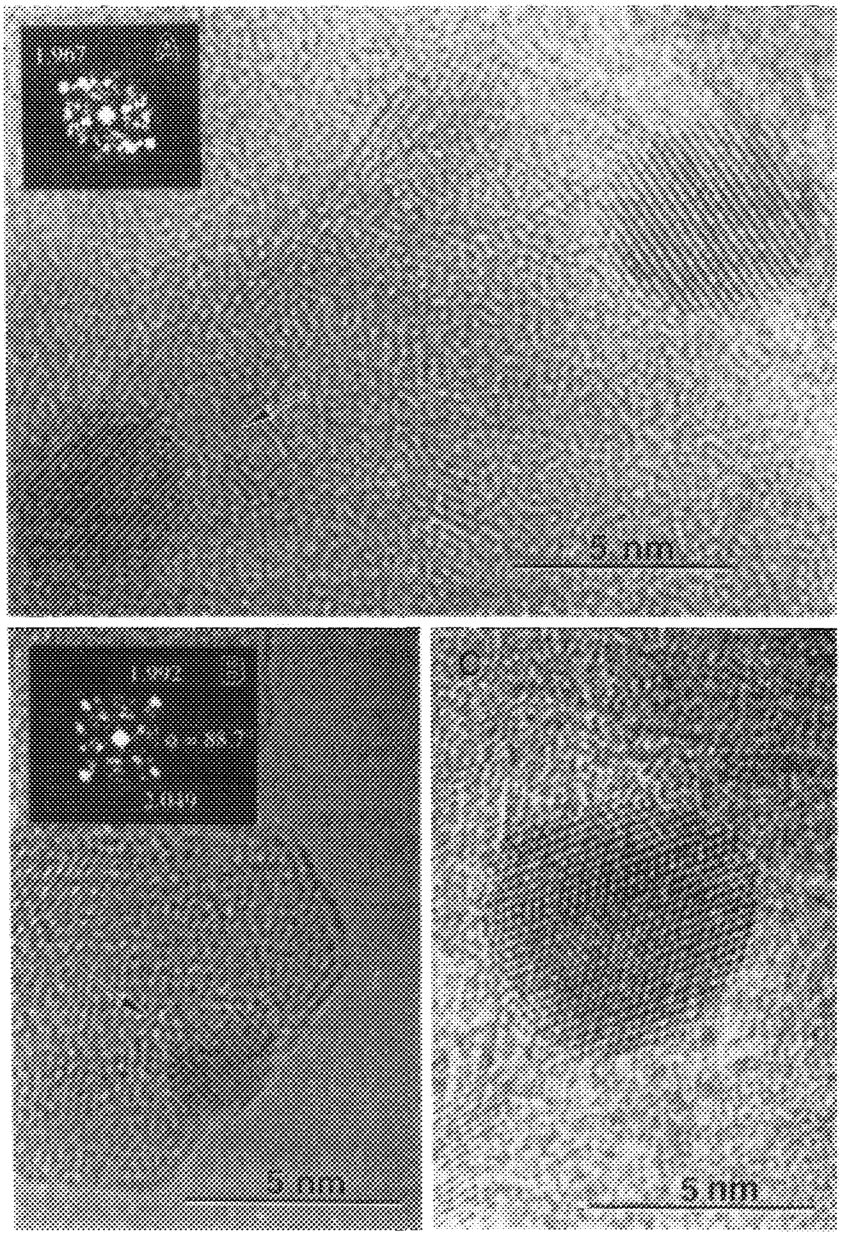

FIG. 7. High-resolution electron microscopy images of the 60/40 catalyst.

The XPS surface composition result for the 60/40A catalyst was 54 wt% Pt (46 wt% Rh). When compared to the expected bulk composition of 60 wt% Pt, this data suggests that the alloy particles of the 60/40A catalyst are only modestly surface-enriched with Rh.

### *95/5 and 17/83 Catalysts*

From the previously described characterization experiments, it became clear that interpretation of the catalytic performance data from the 60/40 catalysts would be difficult because of the broad range of particle compositions which these catalysts contained. There is no basis to assume that Pt-rich, Rh-rich, and 50/50 alloyed particles would perform equally for the same reaction. Therefore, the goal of the following preparations was to make catalysts with simple, well-defined particle composition distributions so that catalytic performance could be determined as a function of particle composition.

The target compositions were chosen to match the prominent compositions of the bimodal particle composition distribution of the 60/40 catalyst (as shown in Fig. 5). These alloy catalysts, identified as the 95/5 and 17/83 catalysts, were first impregnated with Pt precursor, air-dried overnight, and calcined in air at 500°C for 3 h. The materials were then impregnated with Rh and air-dried overnight. Before characterization, the catalysts were reduced in flowing $H_2$ at 300°C for 12 h.

Each catalyst was analyzed for total metal content by ICPAES (Galbraith Laboratories). The 95/5 catalyst contained 1.42 wt% Pt, 0.078 wt% Rh, and 0.69% Cl. The dispersion of the 95/5 catalyst was determined to be 32%. The 17/83 catalyst contained 0.21 wt% Pt and 1.02 wt% Rh, and was determined to be 80% dispersed.

Analytical electron microscopy results for the 95/5 catalyst are presented in Fig. 8. All particles analyzed were Pt-rich and contained between 80 and 100 wt% Pt. There is a trend toward increased Rh concentration with decreasing particle size.

Figure 9 contains the analytical results for the 17/83 catalyst. An overwhelming majority of the particles were found to be Rh-rich in the composition range of 0 wt% Pt to 30 wt% Pt. These particles were typically 2 nm in diameter or less. Since it is difficult to measure particle dimensions smaller than the probe diameter (approximately 2 nm, full width at one-tenth maximum intensity), these particles were reported to be 2 nm in diameter. All particles larger than 3 nm were found to contain substantially more Pt, but on a number basis represented a small portion of the particle population. Thus, the relative number density of the particles is not adequately described by the AEM data of Fig. 9. To further emphasize this point, annular dark-field (ADF) images of this catalyst are presented in Fig. 10. Clearly, the particle population is dominated by 1- to 2-nm particles, which without exception were found to be Rh-rich. The bias in the AEM data arises because of the experimental difficulties encountered when analyzing particles less than 2 nm in diameter. The larger particles are more easily observed and analyzed. Particles less than 2 nm in diameter are much more difficult to analyze because of their relatively low contrast in ADF images. Also, the electron beam may slightly damage the alumina support material, or cause some contamination which can easily obscure the smaller particles. In these cases, several particles must be attempted before a single acceptable analysis is performed.

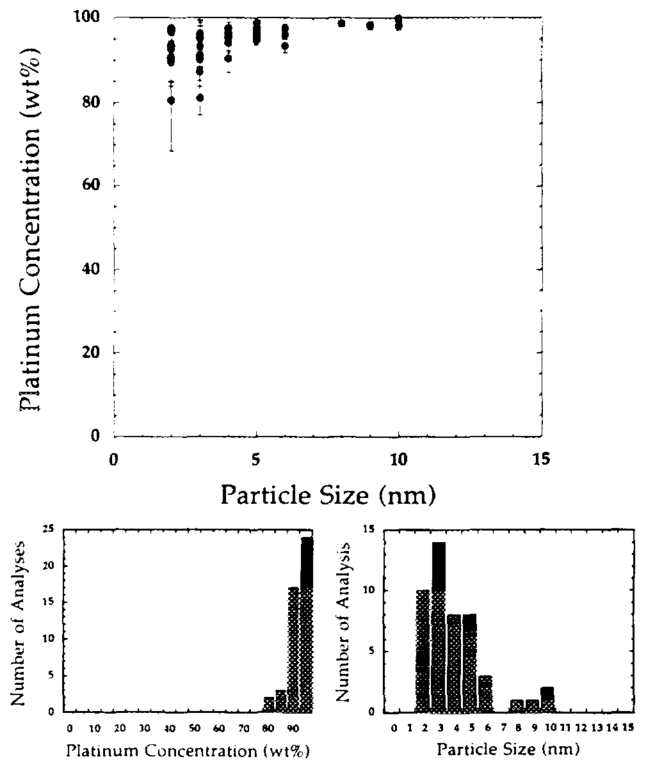

FIG. 8. Plot of particle composition versus size for the 95/5 catalyst. Particle composition and particle size histograms are also presented.

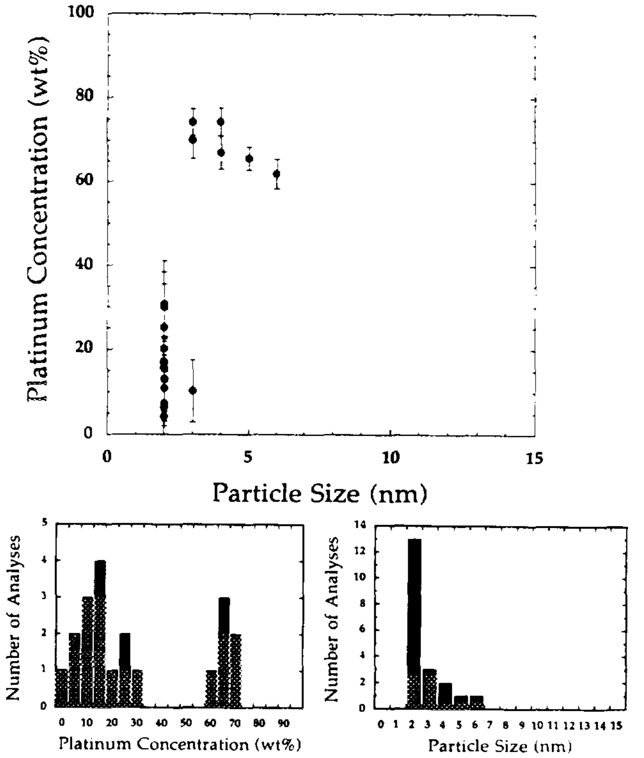

FIG. 9. Plot of particle composition versus size for the 17/83 catalyst.

### *75/25 $Rh_{ox}$–$Pt_{red}$ Catalyst*

This alloy catalyst was first impregnated with Rh, air-dried overnight, and calcined in air at 500°C for 3 h. The material was then impregnated with Pt and air-dried overnight. Unlike previous preparations, the Rh was impregnated first for this catalyst, and then the material was oxidized. The Rh oxidation before Pt impregnation was intended to produce a bimetallic Pt–Rh catalyst with a

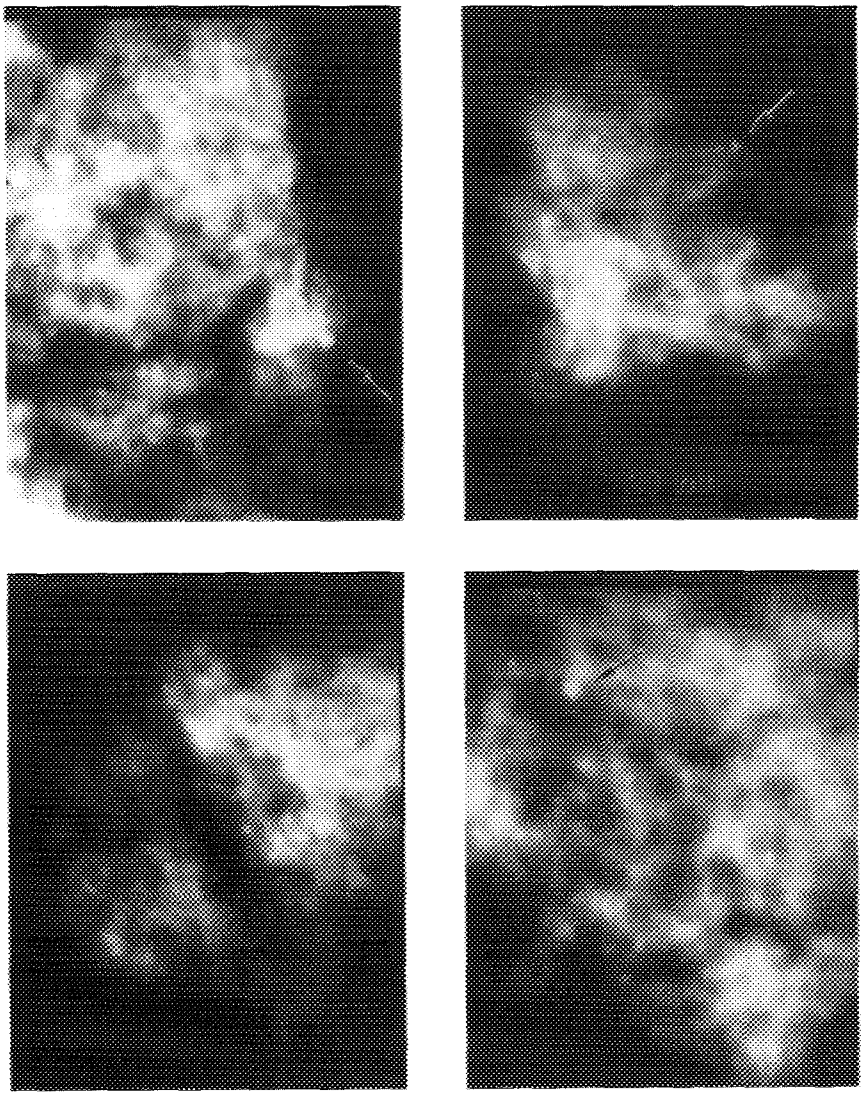

FIG. 10. Annular dark-field images of the 17/83 catalyst which show the large number of Rh-rich particles less than 2 nm in diameter (arrows indicate Pt-rich particle).

minimum of alloying. Low dispersion $Rh_2O_3$ was expected to form, thereby reducing the availability of Rh for alloying. Before catalytic testing, the catalyst was reduced in flowing $H_2$ at 300°C for 12 h. The catalyst was analyzed for total metal content by ICPAES (Galbraith Laboratories) and was found to contain 1.18 wt% Pt and 0.39 wt% Rh. This catalyst was measured to be 55% dispersed.

Analytical electron microscopy results for this catalyst are presented in Fig. 11. The particle composition distribution is dominated by the presence of Pt-rich particles with Pt concentrations greater than the average bulk concentration of 75% Pt. Not presented in Fig. 11 are large particles, up to 200 nm in diameter, that were Rh-rich. Also, XPS results from this catalyst suggested the presence of mixed oxidation states for Rh (Fig. 4b). A portion of the signal intensity from the Rh 3*d* lines was shifted to higher binding energies. This implies the presence of $Rh_2O_3$, possibly associated with the relatively large Rh particles that were observed by AEM.

### *Coimpregnated 72/28 Catalysts*

A single solution which contained both metal salts was prepared, impregnated into the support material, and allowed to air dry overnight. The dry catalyst material was divided in half. One half of the material was reduced in $H_2$ at 300°C for 12 h, and the other half was oxidized in air at 500°C for 3 h. Both catalysts were measured to contain 0.73 wt% Pt and 0.29 wt% Rh.

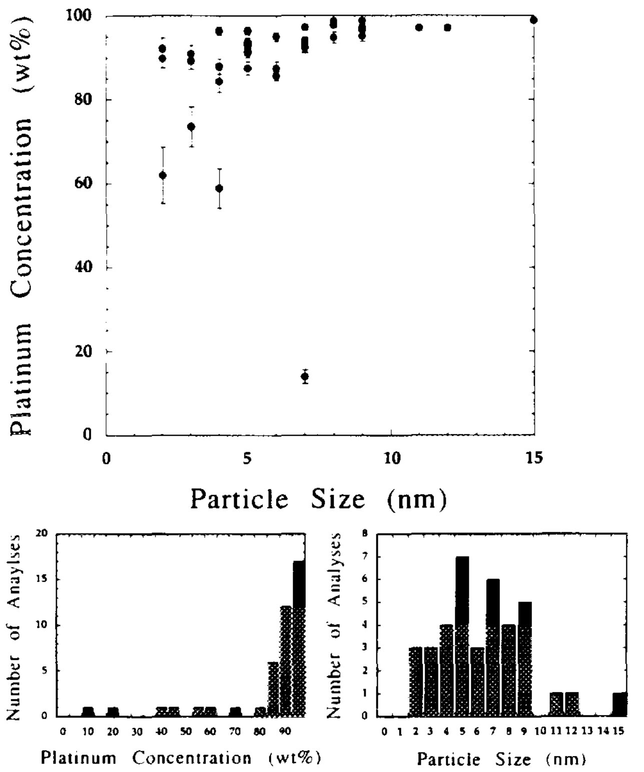

FIG. 11. Analytical electron microscopy results for the 75/25 $Rh_{ox}-Pt_{red}$ catalyst.

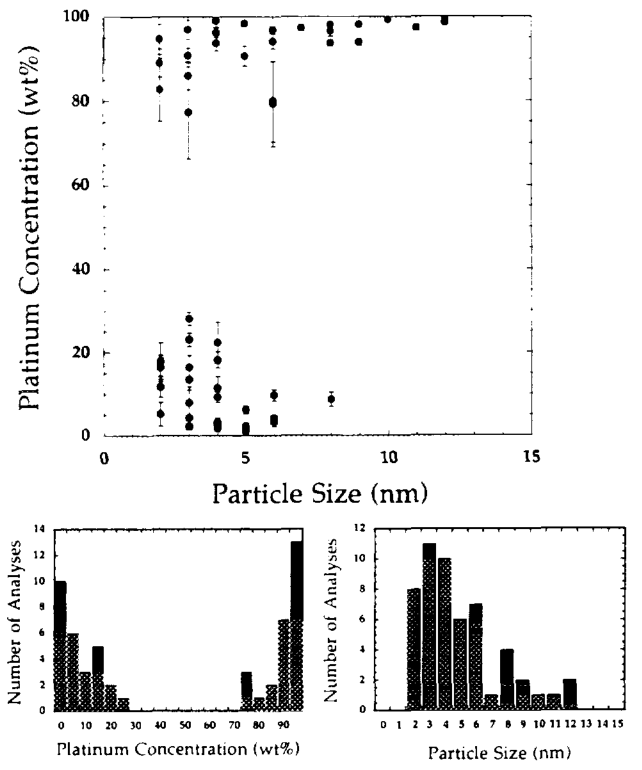

FIG. 12. Analytical electron microscopy results for the 72/28 coimpregnated-oxidized catalyst.

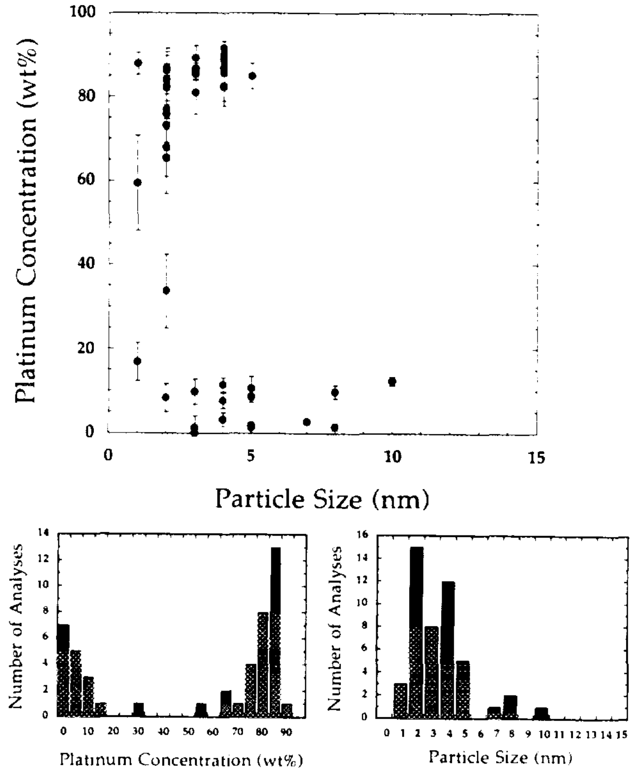

FIG. 13. Analytical electron microscopy results for the 72/28 coimpregnated-reduced catalyst.

Analytical electron microscopy results for the coimpregnated catalysts are presented in Figs. 12 and 13. Both catalysts display bimodal particle composition-size distributions similar to the distribution observed for the 60/40 catalyst. The dispersions of these two 72/28 catalysts were not measured by chemisorption. However, the particle size distributions of these catalysts (Figs. 12 and 13) are quite similar to that of the 60/40 catalyst (Fig. 5) for which the dispersion was 51%.

## DISCUSSION

Particle composition distributions were measured using analytical electron microscopy. Currently, field-emission analytical electron microscopy is the only analytical tool available with the spatial resolution and analytical sensitivity to determine the composition of individual alloy catalyst particles in the 2–15 nm size range. The resulting particle composition distributions presented as a function of particle size have shown that the sequentially impregnated and coimpregnated Pt–Rh catalysts under investigation form alloy particles, and that the particle composition distribution may change as a function of reduction temperature after impregnation. The 60/40 catalyst, which was reduced at 300°C, displayed a bimodal particle composition distribution with few particles between 20 wt% Pt and 60 wt% Pt (Fig. 5). This was an unexpected result. The preparation procedure was selected to produce alloy particles of uniform composition at the bulk ratio of the alloy components (60 wt% Pt). Platinum is known to disperse during oxidation treatment (50–52), and calcination at 500°C is a common preparation treatment which is known to produce highly dispersed Pt catalysts. Rhodium on the other hand, has been shown to coarsen during oxidation (53, 54), and maximum dispersions would be achieved through reduction. In combination, the process of oxidation after Pt impregnation and reduction after Rh impregnation was designed to promote alloy formation.

One possible explanation for the formation of a bimodal composition distribution is the presence of a low temperature miscibility gap (55) in the Pt–Rh equilibrium phase diagram (Fig. 14). The presence of a miscibility gap in the Pt–Rh system was first proposed on the basis of observed miscibility gaps in other group VIII–group VIII binary alloy systems (56), but this phase separation has not been experimentally observed due to kinetic restrictions. If a miscibility gap exists, and if there is sufficient atomic mobility to reach thermodynamic equilibrium, then an alloy which is present at a temperature and composition beneath the miscibility gap would be expected to form Pt-rich and Rh-rich phases as observed (Fig. 5).

If the concentrations at which most particles were observed (peaks in a concentration histogram) are plotted on the phase diagram (Fig. 15), there is good agreement between the AEM data and the proposed location of the miscibility gap. A 50% alloy particle composition would only be permitted at temperatures which approach or exceed the cusp of the gap. This was observed for the 60/40A catalyst which was reduced at 700°C for 72 h (Fig. 6). The fact that there are no well-defined peaks in the 60/40A concentration histogram suggests that the top of the miscibility gap may be near 700°C.

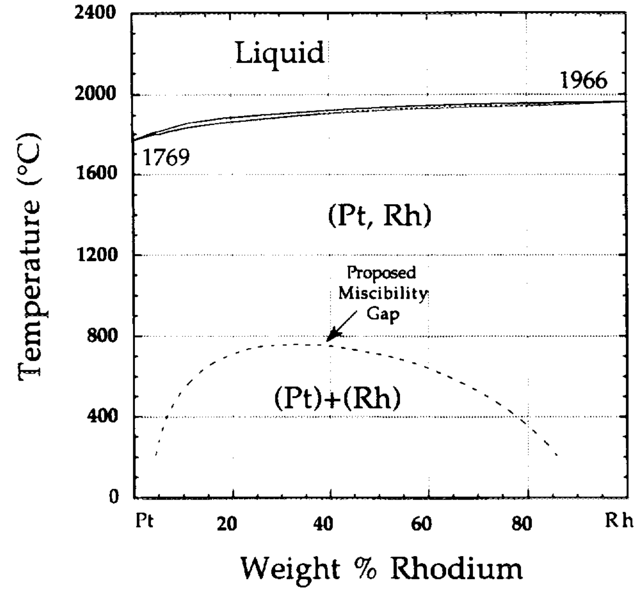

FIG. 14. Pt–Rh equilibrium phase diagram in weight percent Rh which includes the theoretical miscibility gap.

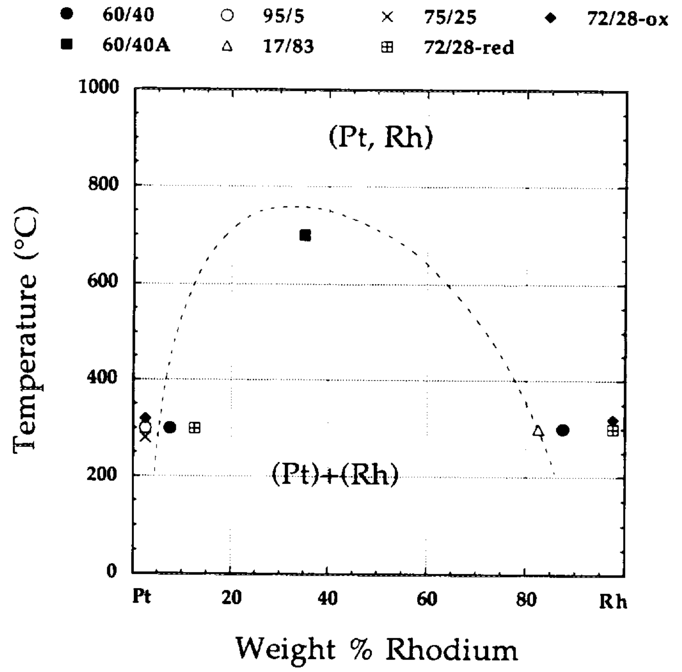

FIG. 15. Pt–Rh equilibrium phase diagram in Rh wt% with data points representing the observed maxima in the AEM particle composition histograms for each catalyst. Multiple data points at 300°C were offset for clarity.

In a bulk system, if a solid solution is cooled below an equilibrium miscibility gap, substantial undercooling may be observed because of the kinetic restrictions of mass transport in bulk metal systems. This is especially the case when the miscibility gap occurs at temperatures less than about half the absolute melting temperature of the alloy. In this low-temperature regime, bulk diffusion in most metals is very limited. When catalysts are prepared, individual metal particles are formed from disordered precursor molecules at temperatures which would permit only limited diffusion in bulk systems. However, it has been previously suggested that when metal particles nucleate from precursor material, they form at an equilibrium concentration simply because there is sufficient atom mobility for them to do so (57). Potential mechanisms for substantial atom mobility in this temperature range include the formation of relatively volatile, and therefore more mobile, Cl complexes or oxides (58).

None of the catalysts prepared for this investigation had particle composition distributions which contradict the Pt–Rh equilibrium phase diagram. The 60/40, 60/40A, 95/5, and 17/83 catalysts were all prepared similarly. For each catalyst, Pt was impregnated, air-dried, and oxidized at 500°C. Following oxidation the Rh was impregnated and reduced at 300°C. Because these catalysts were prepared in a like manner, it may not be surprising that they follow the same path of microstructure development. However, the 72/28 coimpregnated catalysts which were either oxidized or reduced after drying might be expected to behave in a different manner, but they also appear to obey the phase diagram during alloy particle formation. The 75/25 $Rh_{ox}$–$Pt_{red}$ catalyst is the only material that possesses a particle composition distribution which, upon first inspection, appears to contradict the phase diagram. The conflict arises in the lack of Rh-rich particles, and in the general absence of Rh in the 75/25 $Rh_{ox}$–$Pt_{red}$ AEM data. This catalyst was similar in relative composition to the coimpregnated catalysts which had a substantial number of Rh-rich particles in their composition distributions. The apparent absence of Rh is likely due to the formation of $Rh_2O_3$ particles and coarsening caused by the oxidation step in the preparation procedure following Rh impregnation. This conjecture is supported by XPS results which indicate the presence of Rh mixed oxidation states (Fig. 4b), and by the AEM observation of large (100–300 nm) particles that were Rh-rich. Apparently, the oxidation step substantially lowers the Rh dispersion, and effectively reduces the availability of Rh for alloy particle formation. This phenomenon was not observed when the metal precursors were coimpregnated and oxidized together for the same time and temperature (the 72/28 coimpregnated-oxidized catalyst).

XPS has often been applied to catalyst characterization because of the inherent surface sensitivity of the technique and the importance of surface composition to the catalyst investigator. Detailed XPS analyses were performed on the 60/40 and 60/40A catalysts, but before these analyses may be interpreted as the average surface composition of individual particles, the origin of the analytical information must be considered. The depth distribution of measured photoelectrons is described by the inelastic mean free path (IMFP), which is the characteristic path length an electron would travel if its intensity decay is described by the expression (59)

$$I = I_0 \exp(-x/\lambda), \quad [4]$$

where $x$ is the distance an electron has traveled, $\lambda$ is the IMFP for photoelectrons, and $I_0$ and $I$ are the original and final electron intensities. From this relationship, 95% of the signal intensity originates within $3\lambda$ of the surface of the specimen. For this investigation, the inelastic mean free paths are $\lambda_{Pt} = 0.5$ nm and $\lambda_{Rh} = 1.0$ nm (59). Thus, on average, the measured Pt and Rh photoelectrons do not originate from the same depth distribution. For this discussion, it will be assumed that 95% of the signal intensity originates within 3 nm of the metal particle surface. If this is true, an average composition of the entire particle is obtained if the particle radius is less than 3 nm ($3\lambda$). Dispersion measurements, AEM, and HREM indicate that most of the metal particles in the catalysts prepared here were smaller than 6 nm in diameter, and it may therefore be concluded that the XPS data is significantly weighted by the average composition of all the particles less than 6 nm in diameter. Therefore, the XPS signal cannot be considered surface-sensitive for the majority of particles in this study, and must be considered a convolution of small particle overall composition and large particle surface composition.

Compositions determined by XPS for 60/40 and 60/40A were 8 wt% Pt and 54 wt% Pt, respectively. The average particle composition expected from the bulk composition of this catalyst is 60 wt% Pt. Typically, a significantly lower XPS Pt composition from a bulk alloy specimen would be interpreted as surface segregation of Rh. For this investigation, however, when the catalysts are known to possess a complex composition-size distribution with a substantial particle population less than 6 nm in diameter, no reasonable interpretation of surface segregation behavior is possible without additional information. This information must include accurate statistics on the number density of particles in the different regions of the particle composition-size distribution. For this study the shape of the composition distribution has been qualitatively determined, and there are an insufficient number of analyses to infer a number density of particles in any composition or size range. The matter is further complicated in this case because of the large range of observed particle compositions, the nonuniform nature of the distribution, and the possibility of surface segregation. These factors in combination make futile any attempt to unequivocally determine surface compositions of the dispersed particles by XPS alone. The data indicate that the 60/40 catalyst contains substantially more Rh by XPS, because either Rh-rich particles are present at higher dispersion than Pt-rich particles, or the surfaces of all particles are enriched with Rh.

Since the 60/40 and the 60/40A catalysts were physically identical before the final reduction, it may be possible to relate the data from both catalysts and form a self-consistent model of particle microstructure and microstructure development. One potential scenario is that for the 60/40 catalyst which was reduced at 300°C, a portion of the Rh was present at very high dispersion. This scenario would explain the large Rh concentration observed by XPS for this catalyst. In the 60/40A case, when the precursors were reduced at 700°C, the XPS analysis approached the composition anticipated from the bulk metal concentrations. This indicates that Pt and Rh were present in nearly bulk proportions for all particles less than about 6 nm in diameter (this includes most of the particles for this catalyst since it was 44% dispersed). The presence of highly dispersed Rh does not directly contradict the AEM results; it only suggests that AEM was unable to detect highly dispersed Rh particles which may have been present at a particle size less than the imaging and analytical resolution of the instrument (<1 nm). In the case of the 60/40A catalyst which was reduced at 700°C, if Rh were present at high dispersion, this treatment may have provided sufficient opportunity for sintering and alloying of the Rh species with Pt. This could result in the broad composition distribution observed by AEM and predicted by the alloy phase diagram for a composition and temperature near the top of the miscibility gap.

## CONCLUSIONS

1. The composition-size distributions measured during this investigation are consistent with a proposed miscibility gap in the Pt–Rh equilibrium phase diagram. In the past, individual Pt–Rh alloy particles were often assumed to form in relation to the bulk composition. The results of this investigation prove that this assumption can no longer be made. The particle composition distributions that were observed throughout this investigation support the concept that the binary equilibrium phase diagram is useful in predicting the microstructure of dispersed Pt–Rh alloy catalysts. This study also represents the first experimental evidence of a miscibility gap in the Pt–Rh equilibrium phase diagram.
2. HREM found that there are two discrete particle morphologies present in the 60/40 catalyst materials. Particles larger than 7 nm were observed to be faceted along low index crystallographic planes, and are often internally faulted or twinned. Particles smaller than 7 nm displayed no internal faults and appear to be homogeneous, and roughly circular in cross-section.
3. Due to the complexity of the particle composition-size distributions and the high dispersion of the catalysts under investigation, XPS was unable to conclusively determine the surface composition of the catalyst particles. The Pt and Rh photoelectrons measured during quantitative XPS analysis were shown to originate from depths of up to 3 nm in an alloy particle. This implies that the XPS signal represents the bulk composition of all alloy particles less than about 6 nm in diameter. In highly dispersed catalysts this would include most of the particles. Quantitative analysis by XPS does provide a measure of relative metal dispersion in particles less than 6 nm in diameter.

## ACKNOWLEDGMENTS

The authors gratefully acknowledge Dr. Alfred Miller and the Scienta ESCA Laboratory at Lehigh University for their assistance in performing the XPS experiments. We also thank Dr. Waldemar Furdanowicz and the Bethlehem Steel Corporation for their contributions to the AEM experiments. The authors also acknowledge the assistance of Dr. Molly McCartney and the Arizona State University Center for High Resolution Electron Microscopy. This project is supported by the U. S. Department of Energy under contract DE-FG02-86ER45269.

## REFERENCES

1. Armor, J. N., *Appl. Catal.* B **1,** 221 (1992).
2. Hecker, W. C., and Bell, A. T., *J. Catal.* **92,** 247 (1985).
3. Kobylinski, P., and Taylor, B. W., *J. Catal.* **33,** 376 (1974).
4. Stenger, H. G., and Hepburn, J. S., *J. Energy Fuels* **1,** 412 (1987).
5. Hecker, W. C., and Bell, A. T., *J. Catal.* **84,** 200 (1984).
6. Tzou, M. S., Asakura, K., Yamazaki, Y., and Kuroda, H., *Catal. Lett.* **11,** (1) 33 (1991).
7. Oh, S. H., and Carpenter, J. E., *J. Catal.* **98,** 178 (1986).
8. Heezen, L., Kilian, V. N., van Slooten, R. F., Wolf, R. M., and Nieuwenhuys, B. E., *Catalysis Automotive Pollut. Control II* **71,** 381 (1991).
9. Van den Bosch-Driebergen, A. G., Kieboom, M. N. H., vanDreumel, A., Wolf, R. M., van Delft, F. C. M. J. M., and Nieuwenhuys, B. E., *Catal. Lett.* **2,** 73 (1989).
10. Oh, S. H., and Carpenter, J. E., *J. Catal.* **101,** 114 (1986).
11. Sinfelt, J. H., and Cusumano, J. A., (1977) *in* "Advanced Materials in Catalysis" (J. J. Burton and R. L. Garten, Eds.), pp. 1–31. Academic Press, New York, 1977.
12. Schwab, G. M., *Discuss. Faraday Soc.* **8,** 166 (1950).
13. Dowden, D. A., *J. Chem. Soc.* **242** (1950).
14. Dowden, D. A., and Reynolds, P., *Discuss. Faraday Soc.* **8,** 184 (1950).
15. Sinfelt, J. H., Carter, J. L., and Yates, D. J. C., *J. Catal.* **24,** 283 (1972).
16. Sinfelt, J. H., *Adv. Catal.* **23,** 91 (1973).
17. Helms, C. R., *J. Catal.* **36,** 114 (1975).
18. Sinfelt, J. H., *J. Catal.* **29,** 308 (1973).
19. Kim, S. and D'Aniello, M. J., Jr., *Appl. Catal.* **56,** 23 (1989).
20. Kim, S. and D'Aniello, M. J., Jr., *Appl. Catal.* **56,** 45 (1989).
21. Van Slooten, R. F., and Nieuwenhuys, B. E., *J. Catal.* **122,** 429 (1990).
22. Lyman, C. E., Hepburn, J. S., and Stenger, H. G., Jr., *Ultramicroscopy* **34,** 73 (1990).
23. Robota, H. J., Broach, R. W., Sachtler, J. W. A., and Bradley, S. A., *Ultramicroscopy* **22,** 149 (1987).
24. van Delft, F. C. M. J. M., and Nieuwenhuys, B. E., *Surf. Sci.* **162,** 538 (1985).
25. van Delft, F. C. M. J. M., van Langeveld, A. D., and Nieuwenhuys, B. E., *Surf. Sci.* **189,** 1129 (1987).
26. Tsong, T. T., Ren, D. M., and Ahmad, M., *Phys. Rev. B* **38,** 7428 (1988).
27. Ren, D. M., and Tsong, T. T., *Surf. Sci.* **184,** L439 (1987).
28. Ahmad, M., and Tsong, T. T., *J. Chem. Phys.* **83,** 388 (1985).
29. van Delft, F. C. M. J. M., Siera, J., Vreenburg, R. J., van Groos, M. K. K., van Langeveld, A. D., and Nieuwenhuys, B. E., "Proceedings, 9th International Congress on Catalysis, Calgary, 1988" (M. J. Phillips and M. Ternan, Eds.), p. 1114. Chem. Institute of Canada, Ottawa, 1988.
30. Loof, P., Kasemo, B., Anderson, S., and Frestad, A., *J. Catal.* **130,** 181 (1991).
31. Shinjoh, H., Muraki, H., and Fujitani, Y., *Catal. Automotive Pollut. Control II* **71,** 617 (1991).
32. Williamson, W. B., Gandhi, H. S., Wynblatt, P., Truex, T. J., and Ku, R. C., *AIChE Symp. Ser.* **76,** (201), 212 (1980).

33. Wang, T., and Schmidt, L. D., *J. Catal.* **71,** 411 (1981).
34. Van Delft, F. C. M. J. M., Vurens, G. H., Angevaare-Gruter, M. C., and Nieuwenhuys, B. E., *Catal. Automotive Pollut. Control,* 229 (1987).
35. Zhu, Y., and Schmidt, L. D., *Surf. Sci.* **129,** 107 (1983).
36. Chen, M., Wang, T., and Schmidt, L. D., *J. Catal.* **60,** 356 (1979).
37. Lakis, R. E., Cai, Y., Stenger, H. G., Jr., and Lyman, C. E., *J. Catal.*, **154,** 276–287 (1995).
38. Hepburn, J. S., Ph.D. Dissertation, "Analytical Electron Microscopy Studies in the Preparation of Supported Catalysts," Lehigh University, 1989.
39. Micromeritics instruction manual and personal communication, Thomas Hill, Micromeritics Corp., Norcross, GA.
40. Cavanagh, R. R., and Yates, J. T., Jr., *J. Chem. Phys.* **74,** 4150 (1981).
41. Yates, D. J. C., and Murrell, L. L., Prestridge, E. B., *J. Catal.* **57,** 41 (1979).
42. Worley, S. D., Rice, C. A., Mattson, G. A., Curtis, C. W., Guin, J. A., and Tarrea, A. R., *J. Chem. Phys.* **76,** 20 (1982).
43. Yao, H. C., and Rothschild, W. G., *J. Chem. Phys.* **68,** 4774 (1978).
44. Hobbs, L. W., "Introduction to Analytical Electron Microscopy" (J. J. Hren, J. I. Goldstein, and D. C. Joy, Eds.), p. 437. Plenum, New York, 1979.
45. Hren, J. J., "Introduction to Analytical Electron Microscopy" (J. J. Hren, J. I. Goldstein, and D. C. Joy, Eds.), p. 437. Plenum, New York, 1979.
46. Cliff, G., and Lorimer, G. W., *J. Micros.* **103,** 203 (1975).
47. Goldstein, J. I., Costly, J. L., Lorimer, G. W., and Reed, S. J. B., SEM/77, (O. Johari, Ed.) Vol. 1, p. 315. IITRI, Chicago, 1977.
48. Goldstein, J. I., Williams, D. B., and Cliff, G., "Principles of Analytical Electron Microscopy" (D. C. Joy, A. D. Romig, and J. I. Goldstein, Eds.), p. 171. Plenum, New York, 1989.
49. Chojnacki, T. P., and Schmidt, L. D., *J. Catal.* **115,** 473 (1989).
50. Sushumna, T., and Ruckenstein, E., *J. Catal.* **109,** 433 (1988).
51. D'Aniello, M. J., Jr., Monroe, D. R., Carr, J., and Krueger, M. H., *J. Catal.* **109,** 407 (1988).
52. Foger, K., and Jaeger, H., *J. Catal.* **92,** 64 (1985).
53. Lee, C., and Schmidt, L. D., *J. Catal.* **101,** 123 (1986).
54. Gao, S., and Schmidt, L. D., *J. Catal.* **111,** 210 (1988).
55. Moffatt, W., "Binary Phase Diagram Handbook," General Electric Company, Schenectady, NY, 1976.
56. Raub, E. *JLCM* **1,** 3 (1959).
57. Anderson, J. R. "Structure of Metallic Catalysts," p. 265. Academic Press, London, 1975.
58. Ruckenstein, E., "Metal-Support Interactions in Catalysis, Sintering, and Redispersion" (S. A. Stevenson, J. A. Dumesic, R. T. K. Baker, and E. Ruckenstein, Eds.), p. 283. Van Nostrand-Reinhold, New York, 1987.
59. Seah, M. P., and Dench, W. A., *Surf. Interface Anal.* **1,** 1 (1979).